

Improvements in Space Surveillance Processing for Wide Field of View Optical Sensors

Paul F Sydney and Charles J Wetterer
*Integrity Applications Incorporated (IAI) /
Pacific Defense Solutions (PDS)*

ABSTRACT

For more than a decade, an autonomous satellite tracking system at the Air Force Maui Optical and Supercomputing (AMOS) observatory has been generating routine astrometric measurements of Earth-orbiting Resident Space Objects (RSOs) using small commercial telescopes and sensors. Recent work has focused on developing an improved processing system, enhancing measurement performance and response, and supporting new sensor systems and missions.

This paper describes improved techniques in scheduling, detection, astrometric and photometric reduction and calibration, and catalog maintenance. The processing system now integrates with Special Perturbation (SP)-based astrodynamics algorithms, allowing covariance-based scheduling and more precise orbital estimates and object identification. A merit-based scheduling algorithm provides a global optimization framework to support diverse collection tasks and missions. The detection algorithms support a range of target tracking and camera acquisition rates. New comprehensive star catalogs allow for more precise astrometric and photometric calibrations including differential photometry for monitoring environmental changes.

1. INTRODUCTION

Since the deployment of the first small telescopes for space surveillance [1][2], there have been significant improvements in cameras, telescope and mount design, and processing capacity and capability. These advances have allowed the application of new algorithms, techniques, and operating modes for these sensors. Their original mission, collecting astrometric measurements of RSOs for satellite catalog maintenance, has been extended over the years to include RSO characterization using photometric light curves and space debris detection [3][4].

Operations and data reduction for Wide Field-of-View (WFOV) optical sensors for space surveillance can be divided into a series of processes often operating as an autonomous closed-loop system as shown in Figure 1.

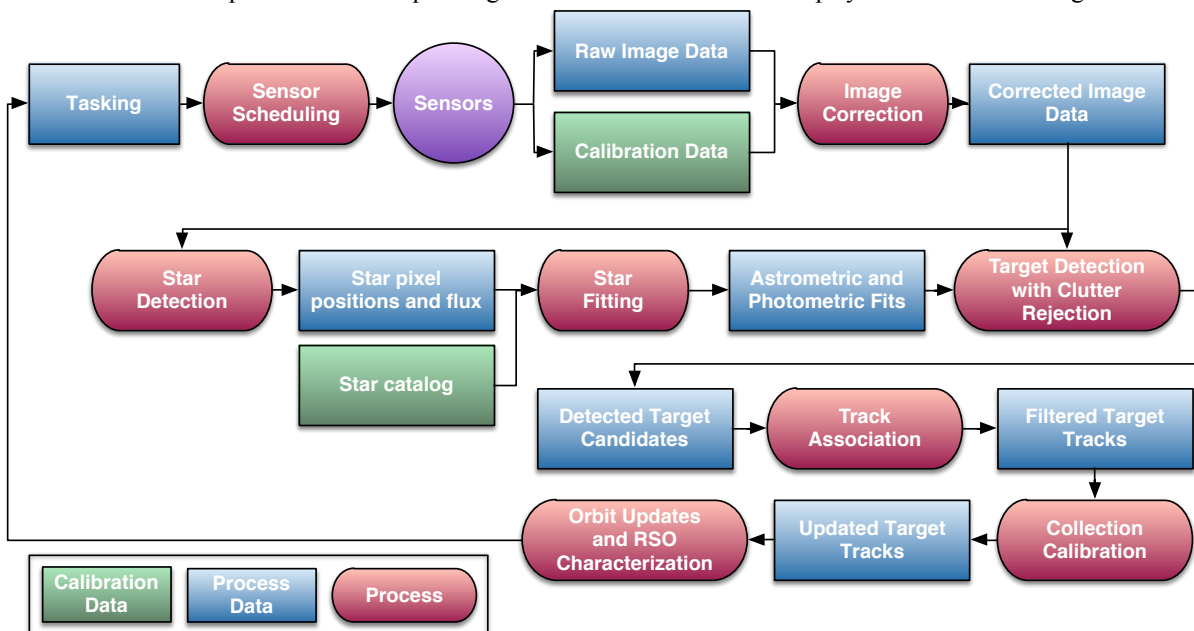


Figure 1. Space Surveillance Processing Flow Overview.

Sensor scheduling involves taking tasking inputs and generating sensor commands to collect images or calibration data. Image correction involves applying calibration data to the input image data to compensate for flaws in the sensor as well as handle dynamic effects such as sky background removal. Using these corrected images, the star detection function extracts star candidates including their position and flux estimates. Combined with a star catalog, the star fitting function determines the astrometric and photometric calibration solutions for each image frame, providing conversions from pixel position and digital number (DN) to equatorial coordinates and in-band brightness. With this fit information, a variety of target detection techniques can be employed to separate a moving object from the image clutter, such as stars and cosmic rays. Once targets have been detected for each image in a collection, a track association algorithm can be employed to match detected objects into a consistent track. Matched target track measurements can be further refined using calibration knowledge and pixel recovery techniques of the entire collection. The calibrated angular position and brightness of each RSO is then processed by an orbit update function for the satellite catalog and RSO characterization tool, producing new tasking as feedback. This paper details a few techniques and enhancements to this processing flow.

2. SENSOR SCHEDULING

Starting with external tasking input [5], the original small telescope scheduler [1] operated by dynamically selecting the next task with the highest priority. If two or more objects had equal high priority, the closest object, minimizing gimbal slew, was selected. The intent was to guarantee that the highest priority objects were observed but this single look-ahead, “greedy” algorithm often resulted in a high priority RSO being observed under poor solar illumination conditions. Phase angle constraints were added to improve detection rates but it still resulted in objects being observed at similar positions in their orbits. For improved orbit determination, there should be diversity and orbital separation in measurements while assuring sufficient Signal to Noise Ratio (SNR) for accurate RSO position measurements [6]. Over the years, there have been improvements in sensor allocation for tasking diversity [7][8], but generally, the scheduler at the sensor has not globally optimized its collection plan to determine the best conditions for each RSO.

To address orbit determination, a new scheduler was developed incorporating an information gain merit for selecting observation times over an entire observation period. Each RSO state error covariance, sensor characteristics, and sensor-target geometry were used to determine the effectiveness of future observations in reducing the uncertainty in orbit estimates [9][10]. Other merit functions were incorporated as well including RSO visibility duration, probability of detection, serendipitous objects, and minimizing gimbal slewing between collections. To maintain RSO state error covariance, Special Perturbation (SP)-based astrodynamics software was incorporated [11]. The computational requirements for generating visibility and SP-based merit functions for a large number of RSOs can be significant and requires the bulk of time in schedule generation [12]. To provide fine visibility time resolution with low computation overhead, the visibility state for each RSO is evaluated sequentially with larger time steps. When a visibility state change is detected, a bisection algorithm is used to determine the fine time resolution within the last large time step. When a large number of RSOs are evaluated, the computational and memory requirements can overwhelm a single compute node. As a result, a parallel catalog scheme with RSOs divided over multiple nodes was developed to support sensor scheduling and orbit updates as shown in Figure 2.

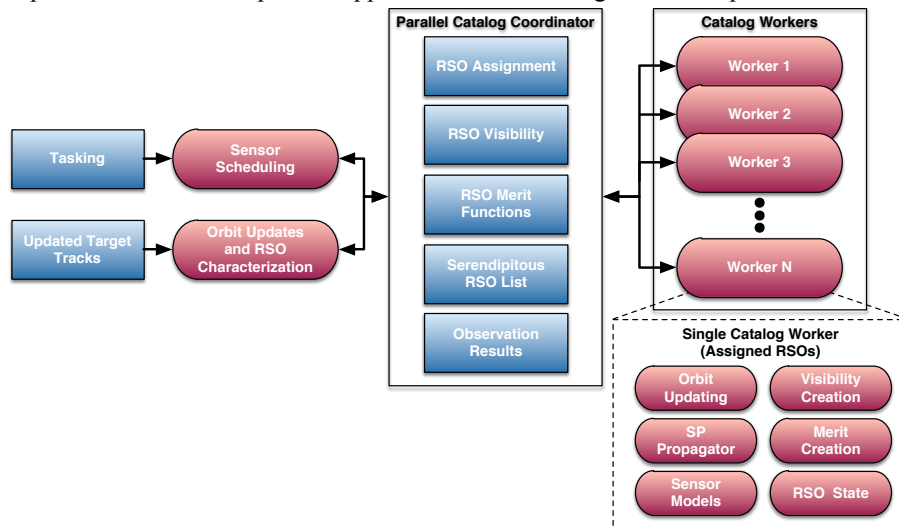


Figure 2. Parallel RSO Catalog Configuration.

With the visibility and merit functions pre-computed, the sensor scheduling can be rapidly updated as dynamic events arise while multiple scheduling realizations can be assessed in the process. As the number of sensors and their missions have grown, the scheduler has evolved to balance multiple sensors and missions with different capabilities and goals simultaneously. Missions, such as RSO characterization [13][14][15], have their own particular collection requirements and cadence. Mission specific merits can be normalized based on their distributions, allowing comparisons between missions while providing higher weights for mission collections with the largest gain. As a result, the total merit of a collection increases from the multiple missions it satisfies.

3. IMAGE CORRECTION

With the schedule generated and a sensor image collected, the image frame is read into the processing pipeline. One of the first steps is to correct for sensor imperfections, such as pixel response non-uniformity. The image-processing pipeline has been updated to use overscan pixels if available. For bias, dark current, and hot pixels, a stack of 50 or more dark images is averaged using a clipped mean algorithm, creating a “Super Dark” frame. However, for a WFOV small telescope, creating an equivalent “Super Flat” frame can be challenging. For large astronomical telescopes, such as Pan-STARRS, sophisticated dome illumination screens providing spectral calibrations have been developed [16][17]. For telescopes without uniform twilight flats, a surrogate “Super Flat” can be generated from 1000 or more images collected with diverse targets and tracking using an iterative clipped mean with outlier rejection. Figure 3 depicts the “Super Dark” and “Super Flat” frames generated using these techniques.

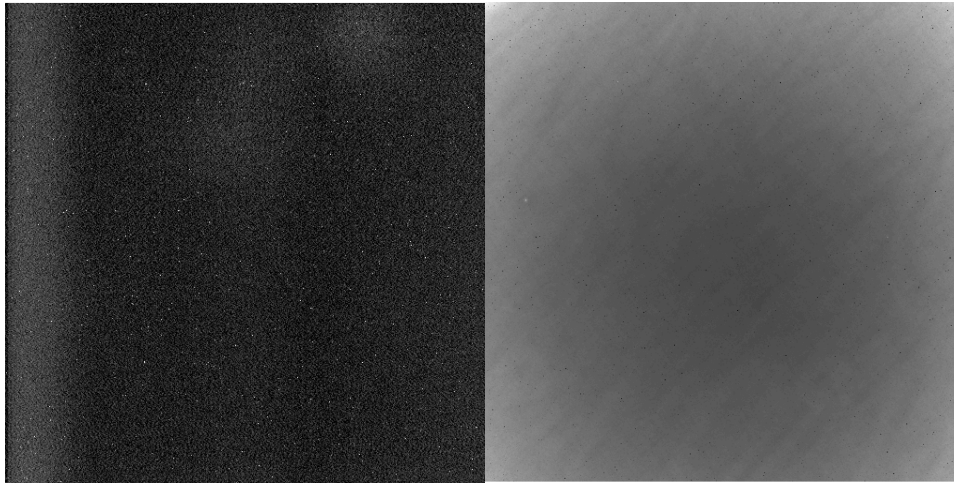


Figure 3. Super Dark and Super Flat Calibration Frames.

Using these calibration frames, Figure 4 shows the original and corrected images with uniformity within 2%, improving the photometric precision across the 0.3° FOV.

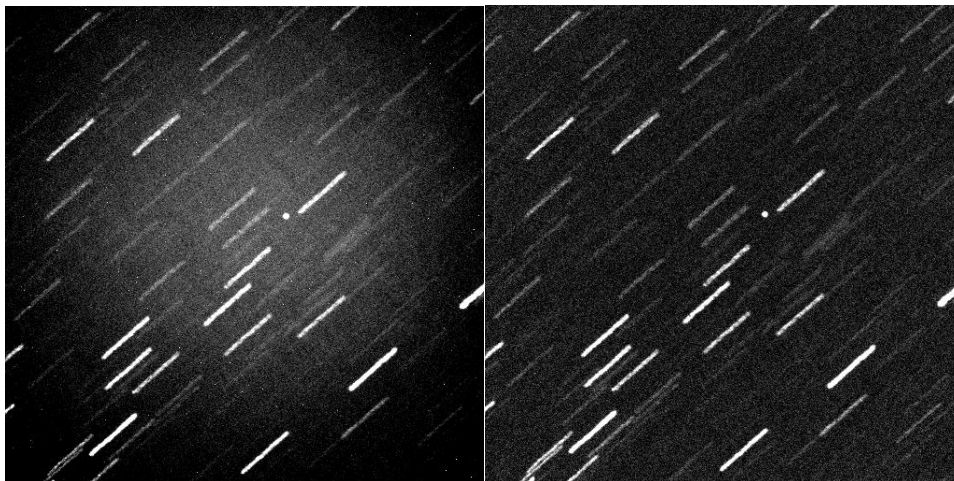


Figure 4. Original and Corrected Images.

When applying flat field corrections, care must be taken to not scale the photon shot noise estimate as well. With the pixel uniformity corrected, dynamic artifacts, such as straylight and sky background, can be fitted and removed from each image frame. Background variations can change rapidly as depicted in the 4 images taken over 40 seconds while tracking a GEO object.

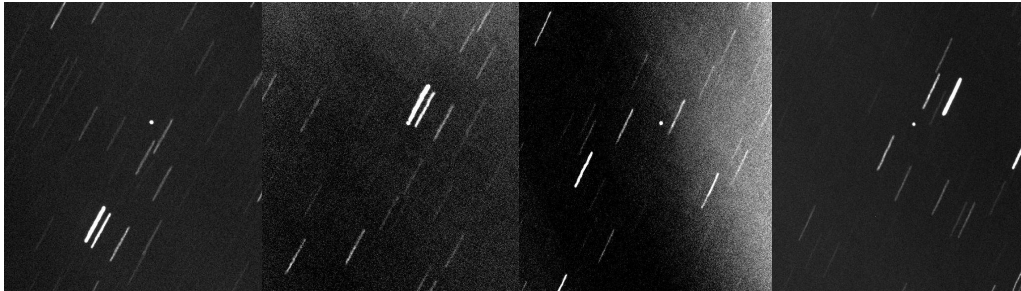


Figure 5. Rapid Straylight Variation for 4 Image Sequence (pixel uniformity corrected) over 40 seconds.

The background-fitting algorithm has remained largely the same and is similar to the method outlined by Bertin [18]. Each image frame is divided into tiles and a percentile value is computed within each tile. A bicubic spline is fit and a background profile estimate is interpolated over the full image as shown in Figure 6.

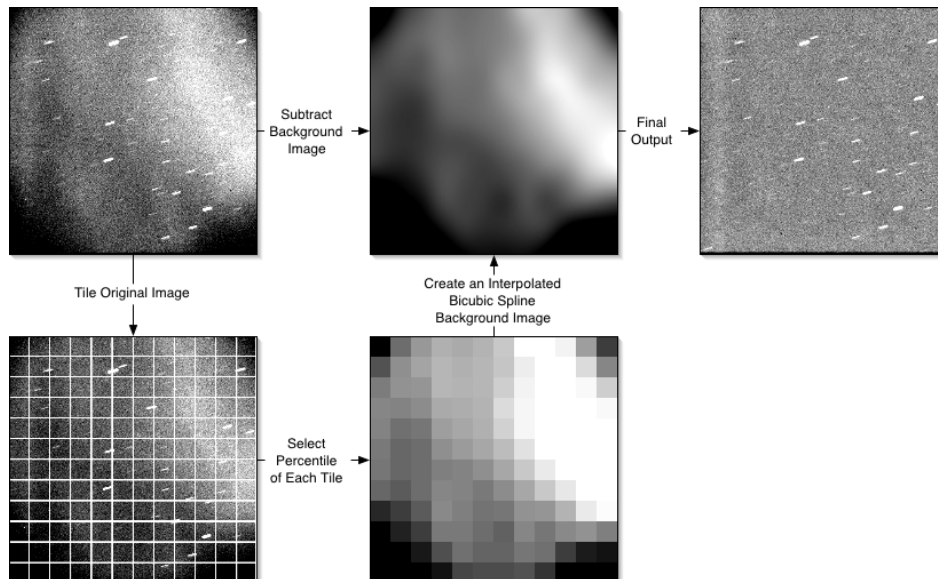


Figure 6. Sky Background Fitting and Removal Algorithm.

One problem with this technique occurs when bright stars skew the statistics within one or more tiles. Since in most cases, the telescope pointing error is less than one milliradian, the bright stars within the sensor FOV are queried based on nominal pointing estimates. A new enhancement excludes tiles within proximity of these bright stars in the spline fit whose area of effect is scaled by the star's brightness. In addition, a linear background fit is always generated and compared to the spline fit to detect outliers. In processing, the background flux is still incorporated in the photon shot noise estimate for detection and detected pixel positions are monitored for new hot pixels.

4. STAR DETECTION

After image correction, stars are detected to provide astrometric and photometric calibration and allow clutter suppression. The star detection methods selected are based on the knowledge of the sensor pointing and imaging Point Spread Function (PSF). In most cases, the sensor-tracking rate is known or can be computed from the RSO ephemeris if tracking at its predicted line-of-sight rate. As an enhancement, one of the first steps that can be applied is a matched filter to increase sensitivity [19]. If the sensor is tracking with sidereal rate or the sensor orientation is unknown, the current imaging PSF can be used as a convolution kernel in the matched filter. In the case of rate tracking with a known sensor orientation, a Streak Spread Function (SSF), combining the PSF and predicted

trajectory trace, can be used as the kernel. If a matched filter is applied, the background noise is estimated directly from the image. Without this filter, the noise is estimated from the known sensor noise, gain, and fitted background profile. In most cases, a simple thresholding algorithm followed by pixel clustering is applied to extract the star pixel clusters. For fast tracking with long star streaks but without a SSF kernel applied, a template-matching algorithm with constrained dilation is used to detect the star pixel clusters. Shape parameters are computed, such as principal axis, for each star pixel cluster and are used to iteratively refine the template when template matching is used.

5. STAR FITTING

Using the star pixel clusters extracted from the image, astrometric and photometric solutions are computed for each image, providing transformations between pixel locations and equatorial coordinates and camera DN to in-band brightness. As an enhancement to refine measurements and support other algorithms, the PSF or SSF can be fit for the star pixels using an iterative non-linear least squares method [20][21]. The fit parameters include x,y position, flux, FWHM, and optionally, local background. With the star measurements established, the next step is to compare with astrometric and photometric star catalogs. The original system relied on the USNO-B catalog [22] merged with the Tycho catalog [23]. It was later superseded with the NOMAD star catalog [24]. Recently, some remarkable new catalogs are being merged and incorporated including the Sloan Digitized Sky Survey (SDSS) [25], Pan-STARRS UberCal [26], and AAVSO Photometric All Sky Survey (APASS) [27] catalogs. These catalog introduce a new set of filter bands defined as SDSS $u'g'r'i'z'$. Pan-STARRS provides another filter band, y' while APASS still includes Johnson B and V filter magnitudes.

With the predicted stars within the sensor FOV retrieved, a pattern-matching algorithm using Gauss' Triangles is applied to match between detected and catalog stars [28]. This algorithm is unchanged from the original system but relies on the 30-50% overlap between the predicted and actual FOVs. To allow for even larger pointing uncertainty, pointing offsets in a spiral search are now iteratively applied to the sensor FOV until the pattern match convergences. Even more robust pattern matching algorithms are being considered for the future that can match star patterns with no pointing knowledge [29][30]. With the measured and catalog stars matched, the next task is to solve for the astrometric transformation. An iterative least squares solver with outlier rejection remains unchanged from the original system, except the 2-dimensional polynomial equations can now be expressed in orders of both Cartesian (x,y) and polar (r,θ) coordinates to better conform with common optical distortion profiles.

The most significant enhancement to sensor processing has been the emphasis on photometric calibration and light-curve generation. A basic photometric transform equation, ignoring color correction terms, can be expressed as:

$$M = m - k'X + z \quad (1)$$

where M is the exoatmospheric magnitude, m is the instrumental magnitude ($-2.5 \log_{10}(flux)$), k' is the atmospheric extinction, X is the airmass, and z is the zero point for the instrument corresponding to the in-band magnitude for 1 camera DN. There are two common methods for photometric calibration. The first method called "all-sky photometry" relies on collecting well-defined photometric stars, such as Landolt UBVRI stars [31][32], measured over a range of airmass values (elevation angles). An equivalent catalog for SDSS $u'g'r'i'z'$ spectral filters has been created by Ivezić [33]. Equation (1) is then solved for k' and z using a weighted linear regression with outlier rejection. All-sky photometry assumes that the atmospheric extinction is consistent over the angular range and time observed. The second method, called "differential photometry," only solves for stars within proximity of the sensor FOV. In this case, an effective zero point, z' is calculated which combines both "all-sky" zero point and extinction values or $z' = z - k'X$. For differential photometry, z' can be solved as $z' = M - m$ using a weighted mean with outlier rejection and histogram analysis. Differential photometry can be computed for any direction in the sky, has less sensitivity to atmospheric changes, and can provide better accuracy, but relies on well-calibrated filter magnitudes for the catalog stars used [34]. With new catalogs being completed such as Pan-STARRS Ubercal [26], photometric calibration stars may soon be available in the entire Northern Hemisphere. With recent changes, sensor processing computes both differential photometry for all images and all-sky photometry when Landolt or Ivezić stars are matched in their catalog filters.

6. TARGET DETECTION WITH CLUTTER REJECTION

After a sequence of images have been calibrated using catalog stars, a target detection algorithm using either single or multiple frames is selected based on the percent overlap of aligned images in a stack, registered by their equatorial coordinates. This overlap percentage varies based on the sensor FOV, telescope tracking rate and relative target rates, and image exposure and readout times. The multi-frame algorithm, depicted as the "Moving Object

Detection” step in Figure 7, is based on combining a stack of N registered image frames in Constant False Alarm Rate (CFAR) pixel detection with Threshold to Noise Ratio (TNR) defined as:

$$P_{\max} - P_{\text{avg}}(\text{w/o max}) > TNR \cdot \sigma_p(\text{w/o max}) \quad (2)$$

where P_{\max} is the maximum pixel value in the image stack and P_{avg} and σ_p are the mean and standard deviation of the remaining pixels in the stack excluding P_{\max} [35]. Image registration is accomplished using bilinear interpolation which acts as a low pass filter blurring the images pixels while reducing the noise. The resulting detected target pixels from Equation (2) are clustered. Similar to SSF matched filter described in Section 5, a velocity-matched filter for hypothesized target tracks can be applied to improve sensitivity [36][37].

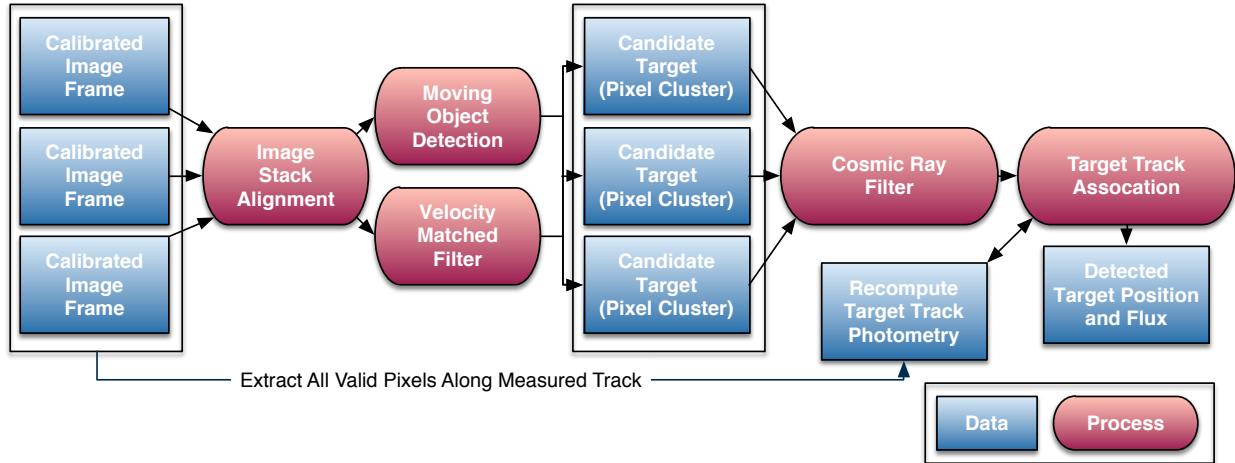


Figure 7. Multiple Frame Clutter Rejection With Stacking.

In general, the multi-frame algorithm requires eight or more frames to compute valid pixel statistics that can result in a reduced effective FOV and limited maximum target rate for detection. For slow camera readouts and fast moving targets, a single-frame detection algorithm was created as an enhancement to allow detection of faster moving objects across the entire FOV. In this algorithm, the image stack is replaced by a synthetic image generated based on the astrometric and photometric solutions, estimated PSF, and catalog stars in the FOV for each individual frame. This algorithm is similar to a method proposed by Hogg [38]. The simulated images provide the mean and standard deviation estimates for applying Equation (2). An example of the algorithm is shown in Figure 8 with the original source frame on the left, synthetic image in the center, and resulting detection pixel clusters on the right with detected RSO and two false alarms.

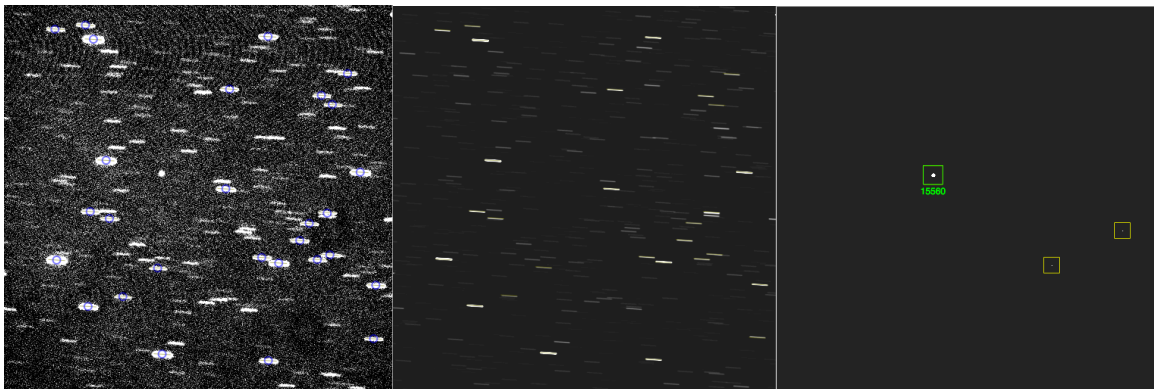


Figure 7. Single Frame Clutter Rejection Using Simulated Image.

The single-frame detection algorithm has worked well in operation provided an accurate PSF can be estimated and tracking jitter is not excessive. This method relies on using a complete star catalog with accurate brightness values,

but variable stars can present a problem. Current variable star catalogs have identified between 43,000 and 324,000 variables stars [39][40][41]. These numbers may be insignificant with respect to the total number of stars in the sky, but many variable stars tend to be brighter in the 8 to 18 visual magnitude range. A cursory scan along the equatorial plane finds 1-10 identified variable stars per square degree. For photometric calibration, outlier rejection ignores these stars. However, in the case of removing star clutter using its predicted flux distribution may result in residual signal and potential false alarms. For identified variable stars, using its measured flux instead can reduce these false alarms.

While the described target detection algorithm can remove most static clutter such as stars, dynamic events, particularly cosmic rays, can generate false target pixel clusters for large format CCDs and long exposure times [42]. To reduce this occurrence, a Laplacian Edge Detection Algorithm for detecting and rejecting cosmic rays was added [43]. The algorithm can be computationally intensive, but by applying the algorithm to pixel clusters produced by the “Moving Object Detection” step in Figure 7, the processing requirements can be greatly reduced.

7. OBJECT TRACK ASSOCIATION

As evident in the detection frame in Figure 8, there can still be false alarms after clutter rejection. To reduce this problem, all candidate target pixel clusters are compared between image frames to form tracks in equatorial coordinates. For most RSOs over short time intervals, this track can be considered nearly linear. For single pixel detection, the probably of false alarm, P_{fa} is related to the TNR by the complementary error function, $erfc(x)$ as:

$$P_{fa} = \frac{1}{2} erfc\left(\frac{TNR}{\sqrt{2}}\right) \quad (3)$$

By requiring M pixel clusters between frames to form a track out of N image frames in the collection, the probability of false alarm for the track, P_{tfa} is reduced as a Binomial distribution to:

$$P_{tfa} = \sum_{k=M}^N \binom{N}{k} (P_{fa})^k (1 - P_{fa})^{N-k} \quad (4)$$

The false alarm rate is reduced as the number of frames in the collection, N is increased, but the M out of N criteria also limits the target rate relative to the line of sight (LOS) that can be detected.

8. COLLECTION CALIBRATION

With all image frames in a collection processed and detected target tracks established, an additional processing stage was added to refine target track measurements, assess long term environmental changes, and refine the calibrations. With each target trajectory known, all pixels along the track can be extracted for each frame based on the exposure times and the measured target flux updated as shown in Figure 7. As noted by Bradley [44], many ground observing sites, such as Haleakala, only have Cloud Free Line of Sight (CFLOS) 40-70% of the time. Differential photometry computed for each image frame can determine when atmospheric transparency has changed as shown in Figure 9, allowing different photometric calibration data combinations with common seeing conditions and probability of detection adjustments for predicted RSO collections.

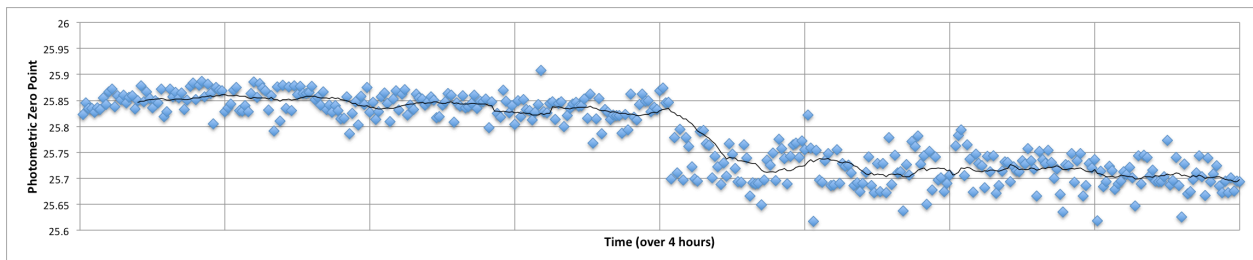


Figure 8. Zero Point Indicating Atmospheric Transparency Change (larger scatter).

For most WFOV space surveillance collections, the same star may be observed over multiple frames. In stable seeing conditions, each star’s flux or instrumental magnitude should remain consistent over the collection. Any flux variation may indicate poor or corrupted RSO measurements. Figure 10 illustrates this effect. The top plot in this figure is an RSO brightness measured over a 9-hour period. The best solar illumination conditions are within the

first hour of observing and increasing solar illumination phase angle results in decreasing the RSO photometric flux as the observing period progresses. In the first 6 hours of observing, the atmospheric conditions remain clear and stable.

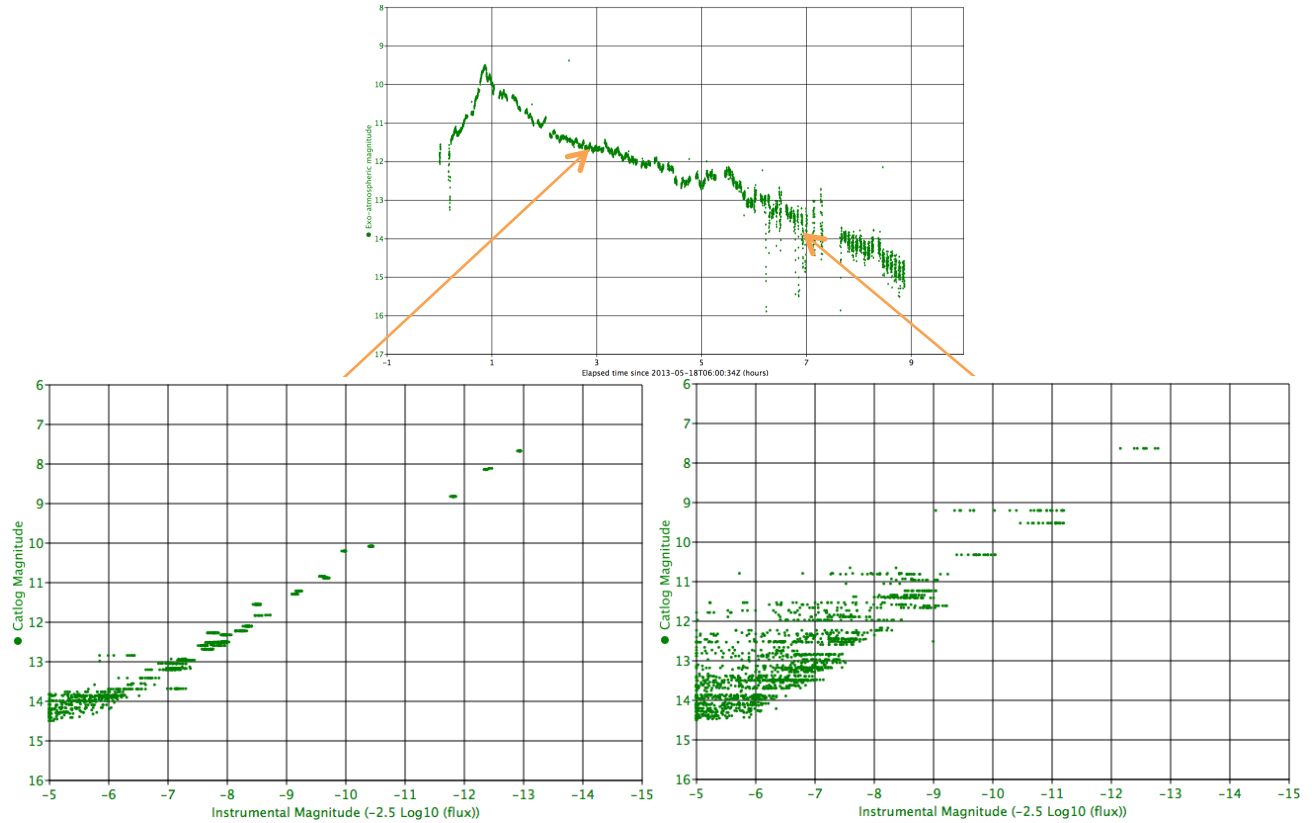


Figure 9. Star Flux Variation Under Varying Seeing Conditions Effecting RSO Signature.

The lower left graph illustrates each star catalog magnitudes plotted vs. its instrumental magnitude (flux) taken over 50 frames. The width of each horizontal line is indicative of measurement errors for each star since it is plotted against its fixed catalog magnitude in the Y-axis. For the brightest stars, the horizontal line width is most narrow and increases in width as the star's brightness decreases. Monet [45] when analyzing Space Surveillance Telescope (SST) collections noted a similar relationship with photometric error increases. The sharp decrease in instrumental magnitude below a catalog magnitude of 14 suggests an increasing flux extraction error near the lowest flux levels. There is evidence that this magnitude limit is not only dependent on the telescope/sensor combination, but also on the tracking rate (i.e. the PSF or size of the SSF of the stars). As noted in the top plot, the RSO measured flux varies rapidly starting after 6 observation hours. The lower right graph plots the same catalog vs. instrumental magnitude comparison for each catalog star as in the lower left graph. However, 7 hours into observing, the horizontal line width has increased dramatically, indicating that the seeing conditions are no longer clear or stable. The benefit of these lower plots is that they provide magnitude error estimates vs. measured magnitude as a function of time and can improve the error estimate in generated photometric data products.

9. ORBIT UPDATES AND RSO CHARACTERIZATION

With the final data products created including RSO position and brightness, the SP-based orbit [11] and RSO characteristics [13] can be updated. Updated orbits and error covariance are input into the scheduler that can adjust the merit functions of each RSO. In addition, updated RSO characteristics may require changes in photometric collection requirements or timing. With these new inputs, the scheduler can dynamically adjust the future sensor collections to provide more valuable measurements and allow the closed loop feedback process to continue.

10. CONCLUSION

The enhancements to space surveillance processing has attempted to maximize the use of information available to provide robust handling of diverse system and environments while improving the quality of its data products. For scheduling, these optical sensors provide more beneficial data while balancing multiple missions. Correction techniques are applied when limited calibration data is available. Comprehensive RSO and star catalogs have enabled more precise calibration and analysis. By continuously monitoring and updating sensor PSF and pointing state, RSO state and characteristics, and environmental conditions such as transmission and straylight, adaptive operations and processing can improve the performance of space surveillance sensors.

11. REFERENCES

1. Sydney, P.F. et al, Raven automated small telescope systems", *Proc. SPIE* 4091, Imaging Technology and Telescopes, 237, October 31, 2000.
2. Sabol, C. et al, *Recent developments of the raven small telescope program*. AAS/AIAA Space Flight Mechanics Meeting, AAS 02-131:397, 2002.
3. Payne, T.E. et al, *Satellite Monitoring, Change Detection, and Characterization Using Non- Resolved Electro-Optical Data From a Small Aperture Telescope*, Advanced Maui Optical and Space Surveillance Technologies Conference (AMOS), Maui, HI, 12-14 September 2007.
4. Shell, J.R., Optimizing orbital debris monitoring with optical telescopes, Advanced Maui Optical and Space Surveillance Technologies Conference (AMOS), Maui, HI, 14-17 September 2010.
5. Wilson, B.L., *Space surveillance Network Automated Tasker*, AAS 04-126, 14th AAS/AIAA Space Flight Mechanics Conference, 8-12 February 2004.
6. Herz, A.F. et al, *SSA Sensor Tasking Approach for Improved Orbit Determination Accuracies and More Efficient Use of Ground Assets*, Advanced Maui Optical And Space Surveillance Technologies Conference, 11-14 September 2013.
7. Miller, J.G., *A New Sensor Resource Allocation Algorithm for the Space Surveillance Network in Support of the Special Perturbations Satellite Catalog*, AAS 03-669, AAS/AIAA Astrodynamics Specialist Conference, Big Sky, Montana, Aug. 3-7, 2003.
8. Miller, J.G., *A New Sensor Allocation Algorithm for the Space Surveillance Network*, 74th Military Operations Research Society Symposium, Colorado Springs, CO, Aug. 28, 2006.
9. Hill, K. et al, *Covariance-Based Network Tasking of Optical Sensors*, AAS 10-150, AAS/AIAA Space Flight Mechanics Conference, San Diego, CA, Feb. 14-17, 2010.
10. Hill, K. et al, *Dynamic Tasking Of Networked Sensors Using Covariance Information*, Advanced Maui Optical And Space Surveillance Technologies Conference, 14-17 September 2010.
11. Hill K., *TurboProp Version 3.0*, Colorado Center For Astrodynamics Research, [http://ccar.colorado.edu/geryon/papers/TurboProp 3 0 Manual.pdf](http://ccar.colorado.edu/geryon/papers/TurboProp%20Manual.pdf), February 12, 2007.
12. Hobson, T. A. et al, *Sensor-scheduling simulation of disparate sensors for Space Situational Awareness*, Advanced Maui Optical And Space Surveillance Technologies Conference, 11-14 September 2011.
13. Hall, D. et al. *Separating Attitude and Shape Effects for Non-Resolved Objects*, Advanced Maui Optical and Space Surveillance Technologies Conference (AMOS), Maui, HI, 12-14 September 2007.
14. Wetterer, C. J. Jah, M.K.. *Attitude Estimation from Light Curves*, *Guidance, Control, and Dynamics*, Vol. 32, No. 5, pp. 1648–1651, September-October 2009.
15. Nishimoto, D. et al, *Satellite Attitude from a Raven Class Telescope*, Advanced Maui Optical and Space Surveillance Technologies Conference (AMOS), Maui, HI, 14-17 September 2010.
16. Tonry, J.; Stubbs, C. and Masiero, J., *The Pan-STARRS PS1 Calibration System*, The Advanced Maui Optical and Space Surveillance Technologies Conference, Maui, HI, September 10-14, 2006.
17. Stubbs, C.W. et al, *Precise Throughput Determination of the PanSTARRS Telescope and the Gigapixel Imager using a Calibrated Silicon Photodiode and a Tunable Laser: Initial Results*, *Astrophysical Journal Supplements Series*, Vol. 191 No. 2, 2010.
18. Bertin, E. and Arnouts, S., *SExtractor: Software for source extraction*, *Astronomy & Astrophysics Supplement* 317, 1996.
19. Alard, C. and Lupton, R.H., *A Method for Optimal Image Subtraction*, *The Astrophysical Journal*, Vol. 503 No. 1, 1998.
20. Press, W. H et al, *Numerical Recipes: The Art of Scientific Computing (3rd ed.)*. New York: Cambridge University Press, 2007.
21. Stetson, P.B., *The Techniques of Least Squares for Stellar Photometry*, Lectures at V Escola Avancada de Astrofisica, 1989.
22. Monet. D.G. et al, *The USNO-B Catalog*, *The Astronomical Journal*, Vol. 125 No. 2, 1998.

23. Hog, E. et al, *The Tycho-2 Catalogue of the 2.5 million brightest stars*, Astronomy&Astrophysics, 355, 2000.
24. Zacharias, N. et al, *The Naval Observatory Merged Astrometric Dataset (NOMAD)*, AAS meeting, San Diego, January 2005.
25. Ahn, C.P. et al., *The Tenth Data Release of the Sloan Digital Sky Survey*, Astrophysical Journal Supplement Series, 2014.
26. Magnier, E.A, et al, *The Pan-STARRS 1 Photometric Reference Ladder, Release 12.01*, The Astrophysical Journal Supplement Series, Vol. 205 No. 20, 2013.
27. Henden, A. et al, *AAVSO Photometric All Sky Survey* (<http://www.aavso.org/apass>), Journal of the American Association of Variable Star Observers, Vol 40, June 2012.
28. Groth, E. J. et al, *A Pattern-Matching Algorithm For Two-Dimensional Coordinate Lists*, The Astronomical Journal, Vol. 91 No. 5, May 1986.
29. Harvey, C., *New Algorithms for Automated Astrometry*, MSc Thesis, University of Toronto, 2004.
30. Hogg, D.W. et al, *Automated Astrometry*, Astronomical Data Analysis Software and Systems XVII, ASP Conference Series 394, 2008, p. 27-34. - Quad hash code.
31. Landolt, A.U., *UBVRI Photometric Standard Stars Around the Celestial Equator: Updates and Additions*, The Astronomical Journal, Vol. 137 No. 5, 2009.
32. Landolt, A.U., *UBVRI Photometric Standard Stars Around the Sky at +50° Declination*, The Astronomical Journal, Vol. 146 No. 5, 2013.
33. Ivezić, Z., Smith, J.A., Miknaitis, G., et al., *SDSS Stripe 82 Standard Star Catalog*, The Astronomical Journal, 134:973-998, 2007.
34. Warner, B.D., *A Practical Guide to Lightcurve Photometry and Analysis*, Springer New York, 2006.
35. Kervin, P.W., et al, *Analysis of Object Observations using a 1.8-meter Telescope*, Fifth European Conference on Space Debris, Darmstadt, Germany, April 2009.
36. Reed I.S. et al, *Optical moving target detection with 3-D matched filtering*, IEEE Trans. Aero. & Elec. Systems, Vol. 24 No. 4, 1988, p. 327-336.
37. Shucker, B. D., Stuart, J. S., *Detecting Asteroids with a Multi-Hypothesis Velocity Match Filter*, Asteroids, Comets, Meteors, Baltimore, Maryland. LPI Contribution No. 1405, 14-18 July 2008.
38. Hogg, D.W. et al, *Astronomical imaging: The theory of everything*, Classification and Discovery in Large Astronomical Surveys, AIP Conference Proceedings 1082, 2008, p. 331–338.
39. Samus N.N. et al., *General Catalogue of Variable Stars*, <http://www.sai.msu.su/gcvs/> (Samus+ 2007-2012).
40. Drake, A.J. et al, *The Catalina Surveys Periodic Variable Star Catalog*, The Astrophysical Journal Supplement Series, Vol. 213 No. 1, 2014.
41. American Association of Variable Star Observers (AAVSO), *The International Variable Star Index*, <http://www.aavso.org/vsx/>, 2014.
42. Smith, A.R. et al., *Radiation events in astronomical CCD images*, IS&T/SPIE's Electronic Imaging, 23 Jan 2002.
43. van Dokkum, P. G., *Cosmic-Ray Rejection by Laplacian Edge Detection*, PASP, 113, 1420 (2001).
44. Bradley, E.S. et al, *Characterization of Meteorological and Seeing Conditions at Haleakala*, PASP, 118:172-182, January 2006.
45. Monet, D. et al, *Rapid Cadence Collections with the Space Surveillance Telescope*, Advanced Maui Optical and Space Surveillance Technologies Conference (AMOS), Maui, HI, 11-14 September 2012.